Operation of terahertz quantum-cascade lasers at 164 K in pulsed mode and at 117 K in continuous-wave mode

Benjamin S. Williams, Sushil Kumar, and Qing Hu

Department of Electrical Engineering and Computer Science and Research Laboratory of Electronics, Massachusetts Institute of Technology, Cambridge, Massachusetts 02139

qhu@mit.edu

John L. Reno

Sandia National Laboratories, Dept 1123, MS 0601, Albuquerque, New Mexico 87185-0601

Abstract: We report the demonstration of a terahertz quantum-cascade laser that operates up to 164 K in pulsed mode and 117 K in continuous-wave mode at approximately 3.0 THz. The active region was based on a resonant-phonon depopulation scheme and a metal-metal waveguide was used for modal confinement. Copper to copper thermocompression wafer bonding was used to fabricate the waveguide, which displayed improved thermal properties compared to a previous indium-gold bonding method.

OCIS codes: (140.3070) Infrared and far-infrared lasers, (140.5960) Semiconductor lasers, (230.5590) Quantum-well devices.

References and links

1. R. Köhler, A. Tredicucci, F. Beltram, H. E. Beere, E. H. Linfield, A. G. Davies, D. A. Ritchie, R. C. Iotti, and F. Rossi, "Terahertz semiconductor-heterostructure laser," Nature **417**, 156 (2002).
2. M. Rochat, L. Ajili, H. Willenberg, J. Faist, H. Beere, G. Davies, E. Linfield, and D. Ritchie, "Low-threshold terahertz quantum-cascade lasers," Appl. Phys. Lett. **81**, 1381 (2002).
3. B. S. Williams, H. Callebaut, S. Kumar, Q. Hu, and J. L. Reno, "3.4-THz quantum cascade laser based on longitudinal-optical-phonon scattering for depopulation," Appl. Phys. Lett. **82**, 1015 (2003).
4. J. Darmo, V. Tamosiunas, G. Fasching, J. Kröll, K. Unterrainer, M. Beck, M. Giovannini, J. Faist, C. Kremser, and P. Debbage, "Imaging with a Terahertz quantum cascade laser," Opt. Express **12**, 1879 (2004). URL http://www.opticsexpress.org/abstract.cfm?URI=OPEX-12-9-1879 .
5. D. C. Larrabee, G. A. Khodaparast, F. K. Tittel, J. Kuno, G. Scalari, L. Ajili, J. Faist, H. Beere, G. Davies, E. Linfield, D. Ritchie, Y. Nakajima, M. Nakai, S. Sasa, M. Inoue, S. Chung, and M. B. Santos, "Application of terahertz quantum-cascade lasers to semiconductor cyclotron resonance," Opt. Lett. **29**, 122 (2004).
6. J. R. Gao, J. N. Hovenier, Z. Q. Yang, J. J. A. Baselmans, A. Baryshev, M. Hajenius, T. M. Klapwijk, A. J. L. Adam, T. O. Klaassen, B. S. Williams, S. Kumar, Q. Hu, and J. L. Reno, "A terahertz heterodyne receiver based on a quantum cascade laser and a superconducting bolometer," submitted to Appl. Phys. Lett. (2005).
7. M. A. Stroscio, M. Kisin, G. Belenky, and S. Luryi, "Phonon enhanced inverse population in asymmetric double quantum wells," Appl. Phys. Lett. **75**, 3258 (1999).
8. B. S. Williams, S. Kumar, H. Callebaut, Q. Hu, and J. L. Reno, "Terahertz quantum-cascade laser at $\lambda \approx 100\ \mu$m using metal waveguide for mode confinement," Appl. Phys. Lett. **83**, 2124 (2003).
9. S. Kumar, B. S. Williams, S. Kohen, Q. Hu, and J. L. Reno, "Continuous-wave operation of terahertz quantum-cascade lasers above liquid-nitrogen temperature," Appl. Phys. Lett. **84**, 2494 (2004).
10. B. S. Williams, S. Kumar, H. Callebaut, Q. Hu, and J. L. Reno, "Terahertz quantum-cascade laser operating up to 137 K," Appl. Phys. Lett. **83**, 5142 (2003).
11. V. B. Gorfinkel, S. Luryi, and B. Gelmont, "Theory of gain spectra for quantum cascade lasers and temperature dependence of their characteristics at low and moderate carrier concentrations," IEEE J. Quantum Electron. **32**, 1995 (1996).

---

12. M. S. Vitiello, G. Scamarcio, V. Spagnolo, B. S. Williams, S. Kumar, Q. Hu, and J. L. Reno, "Measurement of subband electronic temperatures and population inversion in THz quantum-cascade lasers," Appl. Phys. Lett. **86**, 111115 (2005).
13. H. C. Liu, M. Wächter, D. Ban, Z. R. Wasilewski, M. Buchanan, G. C. Aers, J. C. Cao, S. L. Feng, B. S. Williams, and Q. Hu, "Effect of doping concentration on the performance of terahertz quantum-cascade lasers," submitted to Appl. Phys. Lett. (2005).
14. L. Ajili, G. Scalari, J. Faist, H. Beere, E. Linfield, D. Ritchie, and G. Davies, "High power quantum cascade lasers operating at $\lambda \cong 87$ and 130 μm," Appl. Phys. Lett. **85**, 3986 (2004).
15. K. N. Chen, A. Fan, C. S. Tan, R. Reif, and C. Y. Yen, "Microstructure evolution and abnormal grain growth during copper wafer bonding," Appl. Phys. Lett. **81**, 3774 (2002).
16. C.-Y. Chen, L. Chang, E. Y. Chang, S.-H. Chen, and D.-F. Chang, "Thermal stability of Cu/Ta/GaAs multilayers," Appl. Phys. Lett. **77**, 3367 (2000).
17. S. Kohen, B. S. Williams, and Q. Hu, "Electromagnetic modeling of terahertz quantum cascade laser waveguides and resonators," J. Appl. Phys. **97**, 053106 (2005).
18. C. Sirtori, F. Capasso, J. Faist, A. L. Hutchinson, D. L. Sivco, and A. Y. Cho, "Resonant tunneling in quantum cascade lasers," IEEE J. Quantum Electron. **34**, 1722 (1998).
19. M. Chand and H. Maris. Personal communication.
20. J. S. Blakemore, "Semiconducting and other major properties of gallium arsenide," J. Appl. Phys. **53**, R123 (1982).

1. Introduction

The terahertz frequency range (1–10 THz, 30–300 μm) has historically been technologically underdeveloped compared to the neighboring microwave and infrared spectral ranges, despite the fact that it has long been a subject of scientific interest. This is largely due to the lack of convenient techniques for radiation generation and detection. Recently, interest in the terahertz frequency range has exploded, driven in large part by the development of new sources. One such source is the terahertz quantum-cascade laser (QCL), in which photon generation takes place via electronic intersubband transitions in semiconductor heterostructures [1, 2, 3]. Such lasers have already been demonstrated in applications such as imaging [4], spectroscopy [5], and as a local oscillator in a heterodyne receiver [6].

The first terahertz QCL — based on a chirped superlattice design with a novel surface-plasmon waveguide — operated only up to 50 K in pulsed mode, and did not lase at all in continuous-wave (cw) mode [1]. Since that initial breakthrough, major developments have taken place in both the multiple-quantum-well gain medium and the waveguide. Most notably, the resonant-phonon scheme takes advantage of sub-picosecond electron-longitudinal-optical (LO) phonon scattering to selectively depopulate the lower radiative state [7, 3]. Also, the use of a metal-metal ridge waveguide, similar in form to a microstrip transmission line, has been successfully used to provide a high-confinement, low-loss cavity for terahertz lasers [8]. Together, these advances have allowed cw lasing above the liquid nitrogen temperature up to 93 K [9], and pulsed lasing up to 137 K [10].

There is strong interest in pushing operating temperatures to within the range achievable with thermoelectric coolers, and even higher. Achieving intersubband population inversion at terahertz frequencies is difficult because the photon energy $\hbar\omega$ is relatively small ($\sim$10–20 meV), and is not much larger than the low temperature subband broadening ($\sim$4 meV). As a result, obtaining selective injection and depopulation of carriers in the closely spaced upper and lower radiative subbands is difficult, a problem which becomes worse for higher electronic temperatures and as level broadening increases. Furthermore, unlike mid-infrared QCLs, in terahertz QCLs $\hbar\omega$ is less than the LO phonon energy ($E_{\mathrm{LO}} = 36$ meV in GaAs), and the gain displays a strong dependence on the electronic temperature due to the thermal activation of nonradiative optical phonon scattering from the upper to the lower radiative state. While this scattering process is energetically forbidden for cold electrons, at high electronic temperatures T_e it is expected to dominate the upper state lifetime, which takes the form $\tau_u^{-1} \approx \tau_{\mathrm{hot}}^{-1} \exp[(\hbar\omega - E_{\mathrm{LO}})/k_B T_e]$,

where τ_{hot} is the scattering time of an electron in the upper radiative subband with sufficient in-plane kinetic energy to emit an LO-phonon. Finally, thermal backfilling of the lower radiative state by carriers from the injector states reduces population inversion at high temperatures. These effects all depend sensitively on the device electronic temperature during operation, which, as expected, is significantly higher than the lattice temperature during operation due to the finite energy relaxation rate [11, 12]. However, analysis of the performance of existing resonant-phonon lasers suggests that to this point, while these effects degrade laser performance and lead to increased threshold current densities J_{th}, they have not set fundamental limits on laser performance. Rather, device operation ceases at high temperatures when J_{th} reaches the maximum achievable current density J_{max} in a given design [9]; beyond this peak bias point, the injection subbands become misaligned with the upper radiative level and the device enters a negative differential resistance (NDR) regime. While increasing the doping level can increase J_{max} [13], this comes at the cost of also increasing free carrier absorption inside the active region, which is very strong at long wavelengths. Hence, the design challenge is to increase J_{max} without also increasing J_{th}, which would otherwise prevent any net improvement in temperature performance.

In addition to the issues discussed above, high temperature continuous-wave operation requires attention to thermal management, particularly for metal-metal waveguide devices, which are fabricated through a metallic wafer bonding and substrate removal technique [8]. High quality wafer bonding is essential, since unless the devices are mounted top-down, heat removal from the active region must occur through the bonding layer directly below the laser ridge. In our previous work, an indium-gold reactive bonding technique was used to obtain cw operation up to 93 K [9], and thus is capable of providing reasonably good heat sinking. However, while this type of wafer bonding is mechanically robust, the thermal conductivity of the resulting In-Au alloyed layer depends on the metallurgy, and careful control is needed to prevent the formation of voids in the bonding layer. Even under ideal circumstances, the thermal conductivity of the indium-gold alloy cannot approach that of a pure metal such as copper, for which $\kappa \approx 4$ W/cm·K for 100–300 K. In this paper we report the fabrication of metal-metal waveguides using a thermocompression copper-copper bonding technique. By combining this fabrication with an improved active region design, operation of a 3 THz QCL is observed up to 164 K in pulsed mode and 117 K in cw mode.

2. Design and fabrication

The active region of this resonant-phonon laser is composed of 178 repeated periods of the 4-well module grown via molecular beam epitaxy (MBE) in the GaAs/Al$_{0.15}$Ga$_{0.85}$As material system. The conduction band diagram is shown schematically in Fig. 1(a) at the designed bias of approximately 55 mV/module. Lasing is designed to occur between levels $n = 5$ and 4, and depopulation of the lower state occurs via sub-picosecond electron-LO-phonon scattering out of the anticrossed states $n = 3$ and 4 into the collector/injector states $n = 1$ and 2. This active region design is similar to the one described in Ref. [9], except that the injection barrier has been thinned by 2 monolayers from 55 Å to 49 Å. Thinning the injection barrier has the effect of increasing the coupling (i.e. anticrossing gap) between the injector states and the upper radiative state $n = 5$, which results in an increase of J_{max}. However, this change brings the trade-off of decreasing the injection selectivity, and increasing the parasitic current into states $n = 3$ and 4. In order to mitigate this effect, the intra-injector barrier was thickened by one monolayer from 30 Å to 33 Å in order to decrease coupling of $n = 1'$ with the states in next module when the device is below design bias. These changes are opposite from the strategy of thickening the injection barrier that was used successfully in a bound-to-continuum design to increase injection selectivity and reduce lasing threshold [14]. Although these changes are
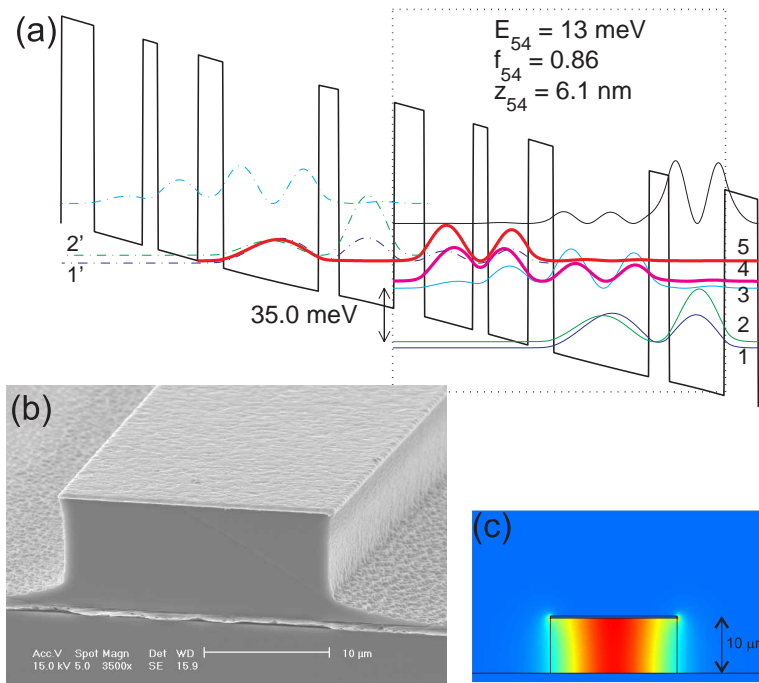
Fig. 1. (a) Calculated conduction band schematic, with the four-well module outlined in a dotted box. Beginning with the left injection barrier, the layer thicknesses in Å are 49/79/25/66/41/156/33/90, and the 156 Å well is doped at 1.9×10^{16} cm^{-3}, which yields a sheet density of 3.0×10^{10} cm^{-2} per module. (b) Scanning electron micrograph of the cleaved facet of a 23-μm-wide ridge waveguide. (c) Modal intensity for fundamental mode calculated with finite-element solver.

relatively modest, because of the small subband energy separations associated with terahertz QCLs, changes of only a few monolayers can have dramatic effects on device performance.

The structure, labeled FL178C-M7, was grown via MBE (growth EA1121) with $n = 5 \times 10^{18}$ cm^{-3} contact layers grown above (50-nm thick) and below (100-nm thick) the 10-μm-thick active region, and with a 200-nm Al$_{0.55}$Ga$_{0.45}$As etch-stop layer underlying the entire growth. The metal-metal waveguide structures were fabricated using a method similar to that described in Ref. [8], except that a Cu-Cu thermocompression bonding technique [15] was used instead of the In-Au reactive bonding method. In this method, both the device wafer and an n^+ receptor wafer were prepared by e-beam evaporation of Ta/Cu (30/500 nm) layers. The Ta layer serves as an adhesion layer and prevents Cu diffusion into the epitaxial layers [16]. The wafers were cleaved into 1 cm^2 dies, and bonding was performed in an EV Group 501 wafer bonder under vacuum at 400°C for 60 min at a pressure of approximately 5 MPa. Following cooling, the devices were annealed for 30 min at 400°C in an N$_2$ atmosphere. Device processing then continued according to the standard recipe. The device substrate was removed by lapping and selective etching, after which standard photolithography could be performed on the 10-μm-thick epitaxial layers. It was observed that dies that underwent the post-bond anneal displayed noticeably fewer stress cracks and defects in the epitaxial layer, which is consistent with previously observed strain relaxation in the copper layer [15]. Compared to the In-Au reactive bonding method, which can be performed by hand on a hot plate, the Cu-Cu method is more demanding in terms of the higher pressures and temperatures required, and is more sensitive to

particulate surface contamination.

Ti/Au (20/400 nm) contacts were deposited and used as self-aligned etch masks to define ridge waveguides via dry etching. Etching was performed in a Plasmaquest electron cyclotron reactive ion etcher using BCl_3:N_2 (15:5 sccm) at 5 mTorr, with a microwave power of 600 W, and an RF power of 15 W. The substrate was thinned to 170 μm to improve heat sinking, and devices were cleaved to form cavities of various lengths, with the facets left uncoated. A scanning electron micrograph of a typical 23-μm-wide ridge structure is shown in Fig. 1(b). The dry etch process results in shallow shoulders at the foot of the mesa which turn out to be helpful in allowing the cleave to propagate properly across the facet. Although the tearing process of the copper that occurs during cleaving obscures the bonding layer somewhat, it is observed to have very few voids, and displays good strength and adhesion, so that wire bonds can be made directly to the top of the ridge.

The intensity profile of the fundamental waveguide mode for a 23-μm-wide ridge waveguide at 3.0 THz is shown in Fig. 1(c). This calculation was performed using a finite-element electromagnetic eigenmode solver (FEMLAB 3.1, Comsol Inc.) according to the methods described in Ref. [17], and using a Drude model for free carrier losses. Drude relaxation times of 0.1, 0.5, and 0.06 ps were used for the heavily doped semiconductor, active region, and gold, respectively. The calculated waveguide loss is $\alpha_w = 18.7$ cm^{-1} with a modal confinement factor of $\Gamma = 0.93$. There is some uncertainty in the value of α_w, since the portion of this loss due to the free carriers in the active region (14 cm^{-1}) is highly uncertain due to the dubious applicability of the Drude model in the multiple quantum well injectors. The metal-metal waveguide is notable for its ability to maintain high confinement factors even for very narrow ridges (less than $\lambda_0/4$), which are advantageous for their low power dissipation.

3. Results

Devices were mounted with In solder on Cu chip carriers and mounted for testing on a cold plate in a vacuum cryostat. The highest temperature operation was observed in a 48-μm-wide, 0.99-mm-long ridge, which lased up to 164 K when biased with 200-ns pulses repeated at 10 kHz. The optical power versus current (*L-I*) characteristics (shown in Fig. 2) were measured with a Ga:Ge photodetector with the laser output severely attenuated so as not to saturate the detector. At 5 K, the threshold current density is approximately 435 A/cm^2, and lasing continues until a current density of $J_{max} \approx 810$ A/cm^2. The inset of Fig. 2 shows the temperature dependence of J_{th}. If this data is fit to the common phenomenological expression $J_{th} = J_0 + J_1 \exp(T/T_0)$, we obtain a value of $T_0 = 56$ K, which is better than for previous devices where $T_0 \sim 30$–40 K [9, 10]. However, such an expression does not fit our data particularly well, and appears to underestimate T_0. This phenomenological characteristic temperature may be better estimated by a simple eyeball fit to the expression $J_{th} \propto \exp(T/T_0)$, which gives $T_0 \approx 130$ K. As can be seen from the inset in Fig. 2, this simple one-parameter fit catches well the asymptotic behavior of J_{th} versus T.

The best continuous-wave performance was obtained from a narrower 23-μm-wide, 1.22-mm-long ridge structure, which lased up to 117 K. This device only lased up to 158 K in pulsed mode, which is likely due to slightly higher waveguide losses in the narrower ridge. The width to wavelength ratio of the device was $w/\lambda_0 \approx 0.22$, which is the narrowest of any laser. In addition to *L-I* curves, voltage versus current (*V-I*), and differential resistance versus current (*dV/dI-I*) characteristics are shown in Fig. 3. Cw spectra were collected using a Nicolet 850 Fourier transform spectrometer with a room temperature deuterated triglycine sulfate (DTGS) pyroelectric detector. Typical spectra taken at several temperatures are shown in the Fig. 3 inset. The observed emission is often single mode, but multiple longitudinal modes were also seen at particular biases and temperatures. Because of the Stark shift of the gain peak,
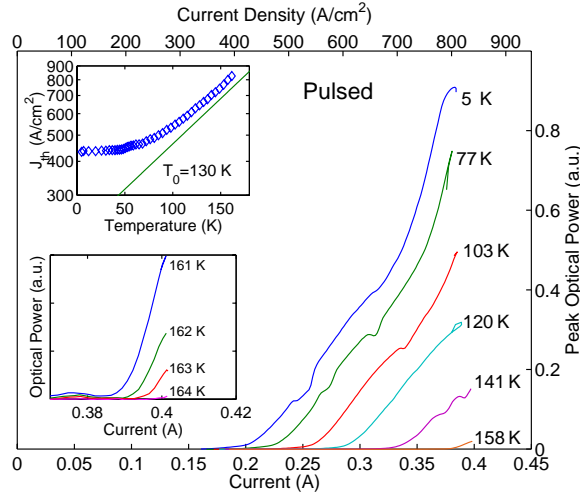
Fig. 2. Optical power versus current measured from a 48-μm-wide, 0.99-mm-long ridge using 200-ns pulses repeated at 10 kHz. The lower inset shows an expanded version of the high temperature *L-I* curves. The upper inset displays the threshold current density versus temperature.

in general the device lases at higher frequency modes at higher temperatures, since the higher lasing thresholds lead to larger electric fields across the structure at the onset of lasing. At a heat sink temperature of 11 K, $J_{th} = 440$ A/cm^2, with a maximum single facet optical power of 2.6 mW (uncorrected for collection efficiency). The output power was collected by a Winston cone placed near the laser facet, and measured with a thermopile detector (ScienTech, Model AC2500) placed directly in front of the cryostat window.

Lasing ceases when the device reaches a current density of $J_{max} \approx 835$ A/cm^2, which corresponds to the bias when the injector states become misaligned with the upper radiative state and the devices enters an NDR region. In addition to the improved value of T_0, part of the reason for the improvement of this laser compared to that from Ref. [9] is that J_{max} is larger by more than 100 A/cm^2, while J_{th} has remained almost unchanged. The fact that J_{max} changes very little with temperature, even as the upper state lifetime τ_5 drops with the increase in thermally activated LO-phonon scattering, suggests that transport is limited by incoherent sequential tunneling through the injection barrier. Thus there may still be more room to optimize performance by thinning the injection barrier even further.

At 11 K, the maximum single-facet wall-plug efficiency is $\sim 10^{-3}$ and the single-facet slope efficiency is measured to be approximately 30 mW/A after correction for the 90% cryostat window transmission. The theoretical slope efficiency in a cascade laser is given by

$$\frac{dL}{dI} = \frac{1}{2}\frac{\hbar\omega}{e}N_{\mathrm{mod}}\frac{\alpha_m}{\alpha_w + \alpha_m}\eta_i,\tag{1}$$

where N_{mod} is the number of cascaded modules in the device, and η_i is an effective internal quantum efficiency that accounts for the injection efficiency of the device, as well as the difference between the upper and lower state lifetimes. It can be shown that under ideal conditions (no residual resistance) η_i is approximately equal to the ratio $\Delta R/R$ discussed below, so we estimate $\eta_i \sim 0.64$ at 11 K. The emitted power is relatively low due to the high facet reflectivity, estimated to be $r \sim 0.85$ [17], caused by the modal impedance mismatch with free space associated with the sub-wavelength waveguide aperture. As a result, the mirror losses are small
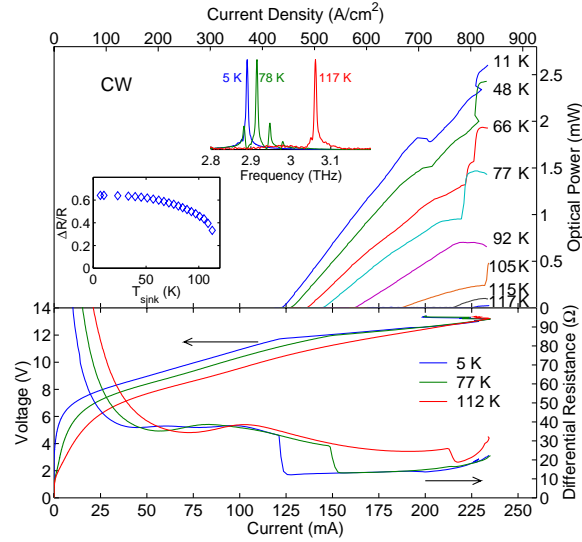
Fig. 3. Continuous-wave characteristics for a 23-μm-wide, 1.22-mm-long ridge at various heat sink temperatures, where the optical power is measured from a single facet. The lower panel displays the V-I and dV/dI-I characteristics at several temperatures. The upper inset shows typical spectra at several temperatures, and the lower inset displays the relative size of the threshold discontinuity in the differential resistance versus temperature.

($\alpha_m \approx 1.3$ cm^{-1}) compared with the waveguide losses (calculated $\alpha_w \approx 18$ cm^{-1}), and a relatively small fraction of the power $\alpha_m/(\alpha_w + \alpha_m) \sim 0.07$ escapes the cavity. This analysis is consistent with the fact that a larger slope efficiency of 60 mW/A (2.7×10^{-3} wall-plug efficiency) was measured from a shorter 23-μm-wide, 0.61-mm-long ridge, due to the fact that its facet losses α_m were twice that of the 1.22-mm ridge.

The differential resistance exhibits a large discontinuous drop at lasing threshold as the population inversion $n_5 - n_4$ becomes clamped at the onset of stimulated emission. The relative size of the discontinuity (shown in the Fig. 3 inset) is a measure of the difference between the upper and lower radiative state lifetimes, as well as a measure of the injection efficiency [18]. In a laser with an empty lower state $n = 4$ (i.e. $\tau_4 \to 0$), and no residual resistance in the injector or at the contacts, the relative change in the differential resistance $\Delta R/R$ would be unity. In our device, $\Delta R/R$ is quite large (~ 0.64) at 11 K, which is a confirmation of the excellent selectivity of depopulation of the resonant-phonon design. A large value of $\Delta R/R$ is an especially desirable feature, since it is approximately proportional to the optical slope efficiency. Even though $\Delta R/R$ drops somewhat as temperature increases, the value of $\Delta R/R$ is still as high as 0.33 at $T_{\text{sink}} = 112$ K in cw ($T_{\text{active}} \sim 150$ K), which indicates that depopulation is still quite selective, and is not yet the limiting factor for achieving high temperature operation. The signatures of the parasitic current channels corresponding to level $1' \to 4$ and $1' \to 3$ transport can be seen in the small local minima in the 5 K differential resistance characteristic at $J \sim 130$ A/cm^2 and 250 A/cm^2 respectively. Although these channels have been greatly suppressed compared to previous resonant-phonon designs [10], further reductions in J_{th} may be possible by further reducing this leakage current.

In order to evaluate how closely the Cu-Cu bonding technique approaches ideal performance, a nonlinear finite-element solver was used to model two-dimensional heat flow out of the laser ridge. The thermal conductivity of the multiple-quantum-well active region was modeled as
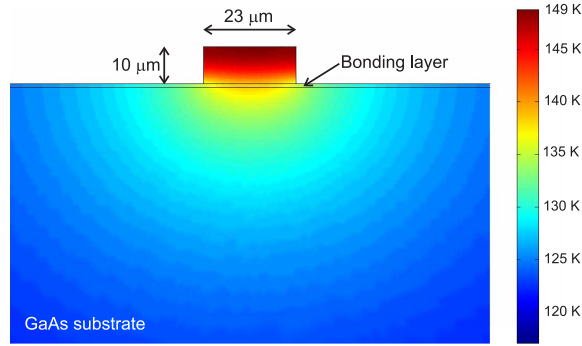
Fig. 4. (a) Two-dimensional heat flow model calculated with a nonlinear finite-element solver. The 800-μm-wide, 170-μm-thick n^+ GaAs substrate extends beyond the margins of the figure. The lower boundary is set to 117 K, and the active region is uniformly driven by a power source of 1.1×10^7 W/cm^3, which corresponds lasing conditions at $T_{\text{sink}} = 117$ K cw operation.

$\kappa_{\text{active}} \approx 0.5$ W/cm·K to correspond with measurements of κ on a similar device [19], the bonding interface was modeled as a 1-μm-thick layer of Cu ($\kappa_{\text{Cu}} = 4.3$ W/cm·K at 150 K), and the n^+ GaAs substrate was modeled with a temperature dependent thermal conductivity according to Ref. [20] ($\kappa_{\text{GaAs}} \sim 2$–1 W/cm·K for 100–150 K). To simulate cw operation at $T_{\text{max,cw}}$, the bottom of the substrate was set to 117 K, and a heat source of 1.1×10^7 W/cm^3 distributed uniformly across the active region. The results are shown in Fig. 4. Because of the high value of κ_{Cu}, thermal resistance of the device is dominated by the temperature drop inside the active region, and spreading resistance in the substrate. The simulated maximum active region temperature is 149 K, 9 K lower than the measured $T_{\text{max,pulsed}} = 158$ K. While the discrepancy may partially arise from uncertainty in the value of κ_{active}, this result suggests that there may be room for improvement in the interface bonding quality. An effective thermal resistance at the peak cw temperature ($T_{\text{sink}} = 117$ K) can be defined for the 23-μm-wide structure, by considering the active region as a lumped element and assuming that lasing ceases when the active region temperature $T_{\text{active}} = 158$ K. This gives a thermal resistance of $R_T = (T_{\text{max,pulsed}} - T_{\text{max,cw}})/P \approx 14$ K/W, where P is the total electrical power dissipated in the device. For comparison, several devices from the same wafer were fabricated with In-Au reactive wafer bonding, and the highest cw temperature that was reached was 76 K.

4.   Conclusion

We have demonstrated terahertz quantum cascade lasers that operate up to pulsed temperatures of 164 K and cw temperatures of 117 K. Improvement over previous designs is attributed to the thinning of the injection barrier in order to obtain a higher peak current density while thickening the intra-injector barrier to prevent an increase in the parasitic current. A copper-copper thermocompression wafer bonding method provided improved heat-sinking capability for laser ridges that consistently allowed higher continuous-wave operating temperatures than devices fabricated with In-Au bonding. Examination of transport characteristics suggest that even at peak operating temperatures, injection and depopulation selectivity remain fairly high, and still higher operating temperatures should be accessible with this design if higher peak current densities could be attained. Furthermore, now that a robust Cu bonding layer is in place, even higher cw temperatures could be reached with more aggressive thermal engineering, such as further lapping of the substrate or electroplating of the sides and top of the ridge with copper or

gold.

Acknowledgments